

Advances in 3D single particle localization microscopy

Cite as: APL Photonics 4, 060901 (2019); <https://doi.org/10.1063/1.5093310>

Submitted: 19 February 2019 . Accepted: 16 May 2019 . Published Online: 04 June 2019

Yongzhuang Zhou , Michael Handley , Guillem Carles , and Andrew R. Harvey 

COLLECTIONS

 This paper was selected as Featured



View Online



Export Citation



CrossMark

ARTICLES YOU MAY BE INTERESTED IN

[Probing micron-scale distributed contortions via a twisted multicore optical fiber](#)

APL Photonics 4, 066101 (2019); <https://doi.org/10.1063/1.5098959>

[A spectrometer for high-precision ion temperature and velocity measurements in low-temperature plasmas](#)

Review of Scientific Instruments 90, 063502 (2019); <https://doi.org/10.1063/1.5092966>

[Nanofocusing on gold planar nanotip arrays](#)

AIP Advances 9, 065103 (2019); <https://doi.org/10.1063/1.5093469>



Alluxa YOUR OPTICAL COATING PARTNER  **DOWNLOAD THE LIDAR WHITEPAPER**

Advances in 3D single particle localization microscopy

Cite as: APL Photon. 4, 060901 (2019); doi: 10.1063/1.5093310

Submitted: 19 February 2019 • Accepted: 16 May 2019 •

Published Online: 4 June 2019



View Online



Export Citation



CrossMark

Yongzhuang Zhou,  Michael Handley,  Guillem Carles,  and Andrew R. Harvey^{a)} 

AFFILIATIONS

School of Physics and Astronomy, University of Glasgow, Glasgow G12 8QQ, United Kingdom

Note: This paper is part of an APL Photonics Special Topic on Computational Optical Imaging.

^{a)}Electronic mail: andy.harvey@glasgow.ac.uk

ABSTRACT

The spatial resolution of conventional optical microscopy is limited by diffraction to transverse and axial resolutions of about 250 nm, but localization of point sources, such as single molecules or fluorescent beads, can be achieved with a precision of 10 nm or better in each direction. Traditional approaches to localization microscopy in two dimensions enable high precision only for a thin in-focus layer that is typically much less than the depth of a cell. This precludes, for example, super-resolution microscopy of extended three-dimensional biological structures or mapping of blood velocity throughout a useful depth of vasculature. Several techniques have been reported recently for localization microscopy in three dimensions over an extended depth range. We describe the principles of operation and typical applications of the most promising 3D localization microscopy techniques and provide a comparison of the attainable precision for each technique in terms of the Cramér-Rao lower bound for high-resolution imaging.

© 2019 Author(s). All article content, except where otherwise noted, is licensed under a Creative Commons Attribution (CC BY) license (<http://creativecommons.org/licenses/by/4.0/>). <https://doi.org/10.1063/1.5093310>

I. INTRODUCTION

Fluorescent point sources are widely used in science and engineering as tracers of velocity fields, indicators of mechanical forces, and labels of biological structures. These applications have aroused broad interest in the past decade, particularly in the life sciences for single-molecule tracking,^{1,2} super-resolution imaging,^{3–5} blood-flow characterization,^{6–8} traction force microscopy,^{9,10} microfluidics,¹¹ and in the development of lab-on-chip devices.^{12,13}

High-resolution microscopy is typified by a restrictively small depth of field (DOF), normally less than the thickness of a single biological cell, and this impedes the probing of three-dimensional behavior of the sample. Even though super-resolution technology has enabled the 2D localization of points to nanometer precision, localization throughout a useful depth range of the third dimension has remained, until recently, a significant challenge.

A number of techniques have emerged in recent years which optically encode the axial position of a particle in the recorded image and additionally enable localization through an axial range that exceeds the conventional DOF. These techniques, together with

their necessary procedures for digitally postprocessing images to recover the positions of particles, encompass the field of 3D localization microscopy. Results from this field have consequently extended super-resolution microscopy for 3D imaging through thick samples and have enabled investigation of the dynamics of biological processes such as blood-flow mapping and 3D single-molecule tracking within a cell. This broad and rapidly advancing field has attracted wide interest in the past decade and several extended reviews provide excellent and detailed overviews, including the following:

- Three-dimensional localization of single molecules for super-resolution imaging and single-particle tracking¹⁴
- Single particle tracking: from theory to biophysical applications¹⁵
- A review of progress in single particle tracking: from methods to biophysical insights¹⁶
- Fluorophore localization algorithms for super-resolution microscopy¹⁷
- Precisely and accurately localizing single emitters in fluorescence microscopy¹⁸

In Secs. II–V, we summarize the key developments in 3D point localization microscopy and compare several techniques using the well-known Fisher-information framework for determining localization precision.¹⁹ We cover some practical methods for position estimation and finish with a perspective on the future of the field. The emphasis here is on fluorescence microscopy, but the principles are equally pertinent to bright-field imaging of scatterers,^{20–22} with the caveat that photon fluxes for bright-field imaging tend to be much higher than those for fluorescence.

The image of a point source recorded by a microscope is characterized by the point-spread function (PSF), which in the diffraction limit has the form of an Airy disk. The resolution and DOF limits of a system are consequently given by

$$d = \frac{\lambda}{2\text{NA}}, \quad (1)$$

$$\text{DOF} = \frac{\lambda}{2\text{NA}^2}, \quad (2)$$

respectively, where NA is the numerical aperture and λ is the optical wavelength. These equations highlight an inverse-square relationship between resolution and DOF, which means that when traditional imaging optics are used, high resolution can be attained only for a small axial range close to best focus.

A well-established method for extending the DOF is to sequentially sweep the focused object plane through the sample³³ to record in-focus images throughout the full sample depth. The so-called focus stacking then enables the computational construction of an image with a very large DOF. However, the time-sequential acquisition renders this technique inappropriate for time-critical experiments, such as where the tracking of moving particles is necessary. In this case, a snapshot method of image acquisition with potential for high frame rates is preferred.

The mostly used 3D single-shot microscopy for precise localization of fluorescent particles are multifocal-plane microscopy (MUM) and PSF engineering. In MUM, several images are recorded simultaneously at different degrees of defocus, and the disparities between the images are used to calculate 3D position of a particle. This is conceptually similar to focus stacking, but instead of incremental refocusing, multiple cameras are focused to several different fixed planes. PSF engineering involves encoding the position of a particle using a nonconventional PSF which exhibits the twin features of varying in some carefully engineered way with defocus, while also enabling recovery over an extended DOF. A detailed description of these methods follows in Secs. II–V.

In this Perspective article, we discuss the principles of operation and the relative merits of the most important techniques used for extended-depth localization microscopy. The key performance metrics are localization precision and the depth range over which high precision can be maintained. We also discuss here the logistics of implementation, the commercial availability, and phase mask fabrication, which may be important to some users. Localization precision is defined as the standard error of a series of measurements of position, whereas localization accuracy is defined as the deviation of the measurement of the mean position from the true position, due to, for example, imperfect calibration or systematic nonisotropic radiation by optical emitters.²⁴

The techniques described herein differ in their optical configurations and in how the 3D position of a particle is encoded by the PSF: for example, by rotation or divergence of the main lobes of the PSF with the range or by a change in form of the PSF. Nevertheless, provided that a suitable model of the image-formation process exists, all techniques can be compared using an information-based description of the measurement of the emitter position. In this way, a theoretical limit of the localization precision can be derived as the Cramér-Rao lower bound (CRLB) of the estimate of the particle position.¹⁹ A full description of this quantity is discussed in Sec. III, where we compare the localization precision of a number of techniques.

II. TECHNIQUES FOR 3D POINT LOCALIZATION

The axial localization of a particle may be estimated simply from the radii of diffraction rings around the defocused Airy disk, as depicted in Fig. 1.^{25–29} Localization of the faint diffraction rings and hence of the particle is relatively poor however, due to the relatively low signal-to-noise ratio (SNR) for the side lobes. The extended PSF also limits the density of defocused particles that can be localized.

Several kinds of estimation procedures achieve improved robustness from the calculation of the defocus parameters of the Airy disks that optimally fit the recorded data³⁰ as discussed in Sec. IV. Localization based on model fitting can be further improved by including more accurate PSF models, such as the Hanser model³¹ and Gibson and Lanni model,³² which account for high-NA scenarios and variations in the refractive index.

A. Multifocal-plane microscopy (MUM)

Following the demonstration of biplane microscopy using two degrees of defocus by Prabhat *et al.*,³³ the concept of multiplane microscopy has since been developed into the wider MUM framework, covering an arbitrary number of focal planes,^{34,35} as

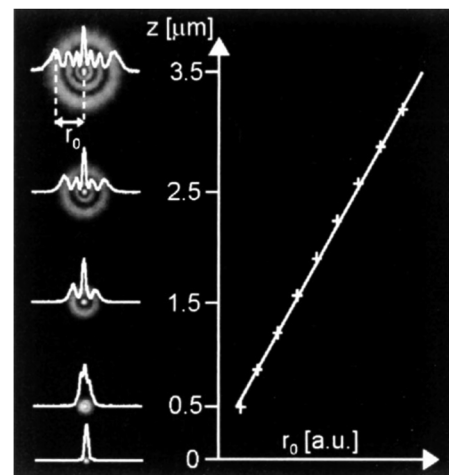


FIG. 1. Depth estimation with an Airy disk. Image adapted with permission from M. Speidel, A. Jonáš, and E.-L. Florin, *Opt. Lett.* **28**, 69–71 (2003). Copyright 2003 Optical Society of America.²⁵

depicted in Fig. 2. The MUM localization algorithm (MUMLA) calculates 3D localization of each particle from correlations of the PSFs recorded in each image.³⁶ A model PSF is fit simultaneously to each image, accounting for the fixed level of defocus between each plane. This results in a more precise estimation of particle position in all three dimensions, owing to the larger information quantity from multiple plane acquisition.

There is a clear trade-off between the localization precision, depth for localization, and the number of planes used to achieve a given axial range. In particular, increasing the number of planes increases the axial range, but the reduction in intensity at each plane due to partitioning the image intensity between each detector degrades the precision.³⁸ A variant of MUM is dual-objective MUM (dMUM),³⁷ which uses two opposing objective lenses in a configuration similar to a 4pi microscope³⁹ (Fig. 2). In this arrangement, twice the amount of light can be collected compared to conventional MUM, which allows for better localization precision.

In MUM, it is inevitable that higher-order aberrations, in particular, spherical aberration, arise due to the differing optical paths and beam splitters for each camera, particularly at high NA. Use of a diffractive multifocal grating (MFG) element, which replicates PSFs onto a single detector with, for example, three or nine differing values of defocus^{40,41} reduces this effect. This technique, termed “multifocus microscopy” (MFM), allows for a simpler optical configuration, employing just a single camera, but the MFG introduces chromatic aberration, which degrades performance and/or restricts spectral bandwidth,⁴² although this can be mitigated using computational techniques.⁴³

A key benefit of MUM is that it can also be used to image extended objects,^{41,44} whereas the emphasis for PSF-engineering

has been on localization of PSFs that are the images of point-like objects.^{45,46} There is also the opportunity to use MUM/MFM in combination with engineered PSFs for even better localization precision, as has been done using an astigmatic PSF^{47–49} and an Airy-beam-based PSF.^{50,51}

B. Digital holography

While our emphasis here is on 3D localization of fluorescent particles, we comment that 3D localization microscopy can also be achieved using holographic reconstruction of light scattered by particles.^{52–57} Holographic 3D localization of amplitude and phase objects, in both reflection and transmission, is possible in a single shot and with a greatly enhanced DOF. Both off-axis^{52,58} and in-line^{53,57} geometries have been reported, although the lower angles between scattered and reference beams in the in-line holography, with associated lower spatial frequencies, are particularly attractive for digital imaging and digital reconstruction of scattered light fields.⁵⁹ We restrict our comments here only to the high-level observations that holographic techniques cannot be used with fluorescent probes, such as those that are used in super-resolution microscopy, and do not benefit from the high-contrast, speckle-free images provided by fluorescence. However, holography offers optimization of SNR through adjustment of the reference wave intensity.

Where particles are used simply as reflective tracers, both holographic and computational imaging techniques can be used. For example, holographic localization of gold nanoparticles has been reported with transverse and axial precisions of 5 nm and 100 nm, respectively, over ranges in excess of 100 μm .^{60,61} This level of performance is comparable to the engineered PSFs described here.

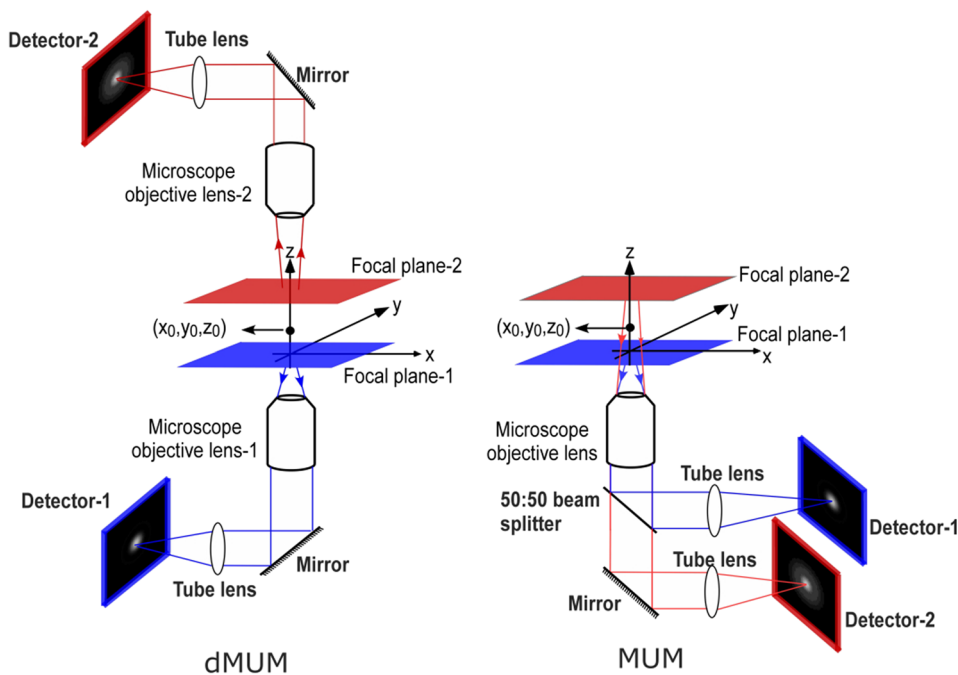


FIG. 2. Multifocal plane microscopy (MUM) and dual-objective MUM (dMUM). Image adapted with permission from Ram *et al.*, *Opt. Express* **17**, 6881–6898 (2009). Copyright 2009 Optical Society of America.³⁷

In this article, we will focus on 3D localization of nanoscale fluorescent emitters using pupil-engineered microscopy. There would be significant interest in a detailed and rigorous comparison between the relative merits of localization using holography with localization using pupil-engineered microscopy of sparse and dense distributions of nonfluorescent particles.

C. PSF engineering

The Airy disk or diffraction-limited PSF (DL-PSF) can be modified by modulation of the amplitude and/or the phase profile of the light field. This is most easily implemented in the pupil plane, where light from an in-focus point source propagates as a plane wave. The amplitude PSF is the Fourier transform of the pupil function multiplied by a z -dependent defocus wavefront^{62,63}

$$PSF_A(x, y, z) = \mathcal{F}\{P(k_x, k_y)e^{ik_z(k_x, k_y)z}\}, \quad (3)$$

where $P(k_x, k_y)$ is the pupil function and $e^{ik_z(k_x, k_y)z}$ is the z -dependent defocus term. For high-NA imaging, $k_z(k_x, k_y) = \sqrt{(\frac{2\pi n}{\lambda})^2 - (k_x^2 + k_y^2)}$, where n is the refractive index between the point source and the objective and λ is the wavelength.⁶³ Thus, to modulate a PSF, a corresponding amplitude and/or a phase profile is introduced into the pupil function, $P(k_x, k_y)$.

In most modern microscopes, the exit pupil is situated inside the objective itself and so it is convenient to reimagine the pupil plane, using a $4f$ relay to an external location where optical modulation can be conveniently introduced. Spatial light modulators (SLM) are popular devices for this purpose since they allow for flexibility in the PSF design, but they suffer from several disadvantages; in

particular: they are expensive and optical efficiency is reduced by the need to operate with polarized light and the diffractive nature of an SLM yields multi-order-diffraction losses. Special optical configurations have been reported to make use of both polarizations;⁶⁴ however, loss through diffraction is inevitable. Fabricated refractive masks yield higher optical efficiency (almost 100% using modern laser polishing and antireflection coating),⁵¹ but without the programmable flexibility of an SLM.

1. Early methods of PSF engineering

Willert and Gharib's three-pinhole mask⁶⁵ predates pupil engineering, but nonetheless succeeds in encoding 3D particle position through the variation in the PSF with axial position. As the name suggests, a mask with a triangular arrangement of three pinholes is placed at the back aperture of the objective (Fig. 3), which produces an array of three spots, which vary in separation according to the axial location of the point source. Originally developed for particle-tracking velocimetry (PTV), this technique has recently found uses in 3D flow characterization,⁶⁶ in sensors for microfluidic devices,⁶⁷ and in the macroscale for tracking the motion of zooplankton.²¹ However, the drawback of using such a mask is that the pinholes block out much of the light.⁶⁸ In fact, phase-only masks tend to be generally favored over amplitude masks because they enable imaging with nearly all of the photon flux. This is particularly important in low-light scenarios, such as for single-molecule imaging.

By far, the most widely used technique for 3D point localization is astigmatic imaging, as evidenced by the wealth of literature which use this method: from micro-PTV^{69–72} to super-resolution microscopy^{73–76} (Fig. 4). Kao and Verkman⁷⁷ were the first to

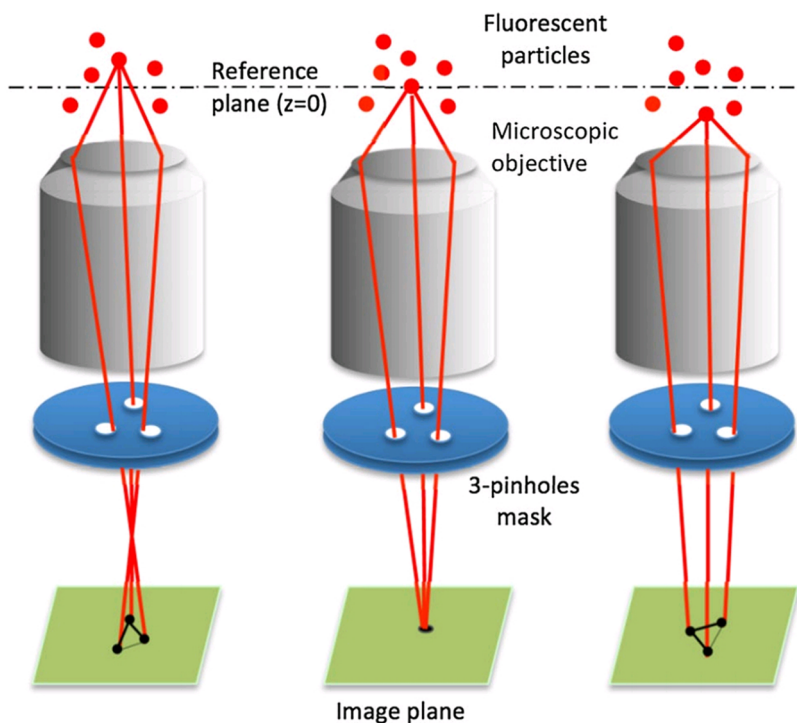


FIG. 3. Schematic of particle localization using the three-pinhole mask. Image adapted from H. Wang and P. Zhao, *Microfluid. Nanofluid.* **22**, 30 (2018). Copyright 2018 Author(s), licensed under a Creative Commons Attribution 4.0 License.⁶⁶

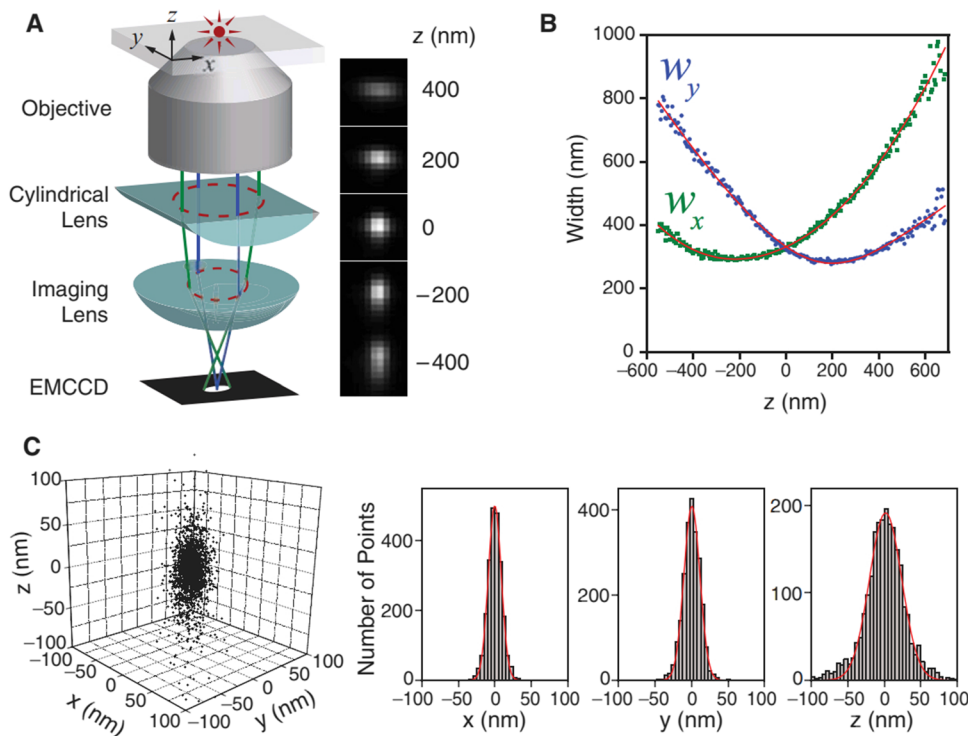


FIG. 4. Astigmatic PSF generated using a cylindrical lens. Image adapted with permission from Huang *et al.*, *Science* **319**, 810–813 (2008). Copyright 2008 American Association for the Advancement of Science.⁷³

use astigmatic localization: they placed a cylindrical lens into the imaging pathway to yield an elliptical PSF whose ellipticity varies with defocus. Following calibration, measurement of the ellipticity directly yields axial and transverse localization. The popularity of astigmatic localization microscopy is due to the simplicity and low cost of implementation (just the cost of an additional simple cylindrical lens). For this reason, analytical models of the 3D astigmatic PSF profile have been derived, which enable better localization precision with more advanced estimation techniques.⁷³

2. Rotating PSFs

Rotating PSFs for depth estimation were first proposed by Greengard *et al.*⁸⁰ A superposition of five Gauss-Laguerre (GL) modes was used to produce the twin-lobe PSF, which continuously rotates around a common center as defocus changes, to describe a double helix. Such a PSF, however, yields low photon efficiency as a large fraction of energy is distributed in the side lobes—typically only 1.8% is contained in the two main lobes used for localization. Pavani and Piestun optimized the design to improve the photon efficiency, resulting in the high-efficiency rotating PSF with 56.8% contained in the two main lobes (HER-PSF).^{78,81} In this design, they used the rotating PSF in Ref. 80 as a first estimation and optimized iteratively in the spatial domain by maximizing the energy in the main lobes of the PSF, in the Fourier domain by constraining the transfer function to be phase-only, and in the GL domain by multiplying the GL modal decomposition with a weight function that boosts the PSF rotation. The optimization process results in about 30 times more energy in the main lobes⁸¹ (Fig. 5),

providing a significant enhancement in performance for photon-limited experiments. Such a PSF was termed the double-helix PSF (DH-PSF) and used for three-dimensional single-molecule imaging.⁷⁸ To avoid the photon inefficiency of an SLM, Grover *et al.* utilized a fabricated phase mask using gray-level lithography.⁸² Such a fabricated phase mask avoids single-polarization modulation and high-diffraction-order photon loss of an SLM, yielding a transmission efficiency of 87%—around twice that of an SLM. It is worth noting that the DH-PSF is perhaps the most widely used 3D localization technique after astigmatism.

Another version of DH-PSF was reported in the “SPINDLE” experiment with the aim of generating the DH-PSF with an analytical expression (the PSF was termed DH-PSF-S).⁸³ The analytical pupil function is formed by a set of vortex singularities on a straight line along a diameter of the pupil, which reduces the PSF design to two parameters: the number of vortex singularities N and the constant spacing d between them. The two parameters were then optimized with respect to the average localization precision (as defined by the CRLB). The DH-PSF-S improves the localization precision for imaging in the presence of high-background signals, but with a compromise in the depth range compared to the original DH-PSF.⁸³

Based on the same optimization process as described in the DH-PSF work, Lew *et al.* reported the design of a corkscrew PSF which yields a single lobe that rotates about an axis with changing defocus of the source⁷⁹ (Fig. 6). The energy in this PSF is more concentrated than the DH-PSF, having only one lobe; however, two measurements with a 180°-rotated phase mask are needed for a single depth estimation because the rotation angle cannot

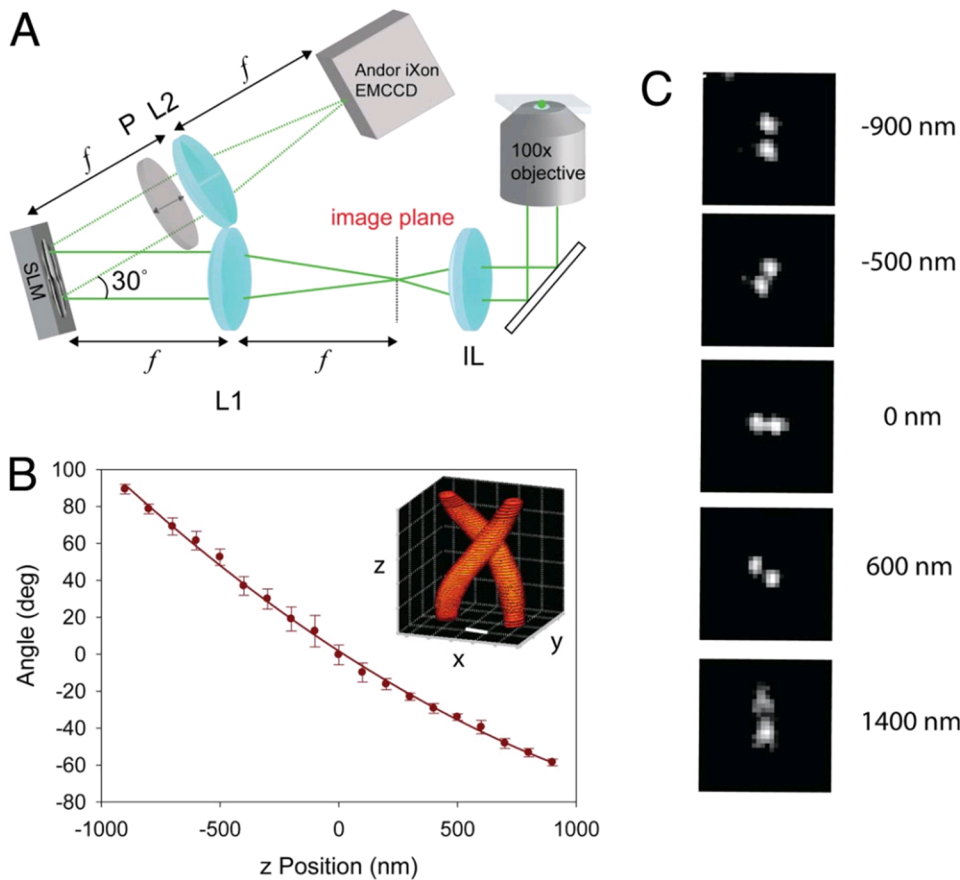


FIG. 5. Double-helix PSF (DH-PSF) with its calibration data and imaging setup. The DH phase mask is introduced using an spatial light modulator (SLM) placed at the Fourier plane of a $4f$ system. Image adapted with permission from Pavani *et al.*, Proc. Natl. Acad. Sci. U. S. A. **106**, 2995–2999 (2009). Copyright 2009 National Academy of Sciences.⁷⁸

be determined from a single image. The sequential image acquisition prevents this method from being applied to super-resolution experiments with blinking dyes as a fluorescent molecule cannot be guaranteed to be emitting during two consecutive frames. It is noted in Ref. ⁷⁹ that two $4f$ sections can be used to avoid the sequential imaging using a biplane approach, although with a

halving in light intensity, which cancels a major advantage over the DH-PSF.

Higher-order helical PSFs such as triple helix and tetra helix have also been reported more recently,⁸⁴ and these have been shown to have superior robustness with respect to optical aberrations. For photon-limited experiments, these higher-order PSFs will yield

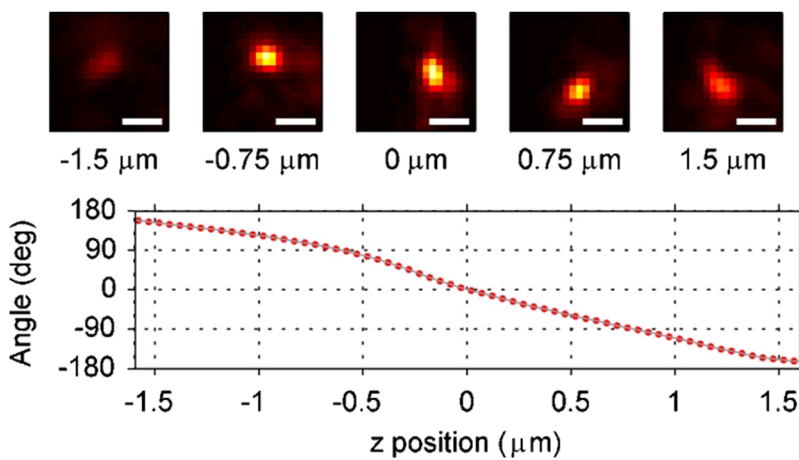


FIG. 6. Corkscrew PSF with its calibration curve. Image adapted with permission from Lew *et al.*, Opt. Lett. **36**, 202–204 (2011). Copyright 2011 Optical Society of America.⁷⁹

lower SNRs, due to the distribution of the energy among a higher number of lobes, but aberration-robust PSFs could potentially offer enhanced localization through refractive or turbid thick biological samples.

3. Translating PSFs

An alternative encoding of axial displacement can be obtained by using several PSFs which translate with defocus. Yajima *et al.* developed a technique for 3D particle localization using a wedge prism located at the back focal plane of the objective, forming two split images at the image plane.⁸⁸ The linear phase introduced by the prism separates the two lobes in the transverse, y , direction.

An axial, z -directed, displacement of the point source is then converted into an x -directed disparity between the two split images. Sun *et al.* subsequently reported a similar, co-called *parallax* technique, using instead two closely spaced mirrors located at a reimaged back focal plane of the objective as shown in Fig. 7.⁸⁷ This offers more flexibility for positioning the split views on the camera chip. The technique was used to study glucose-transporter-containing vesicles in living adipocytes. Another similar technique, the *bisected pupil*, uses an SLM with two linear phase ramps to create a two-lobe PSF.⁶⁴ In this case, two orthogonal linear polarizations of light are recorded to enable correction of localization errors induced by the orientation of the dipole emitters. When imaging isotropic

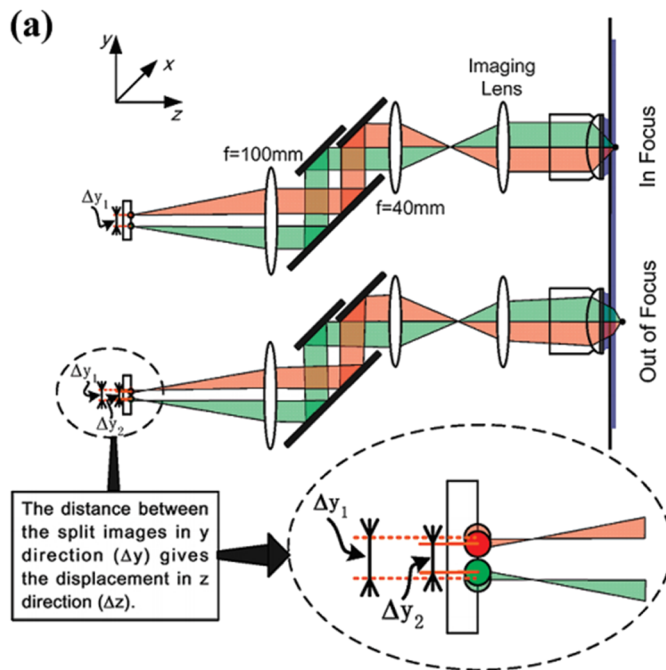
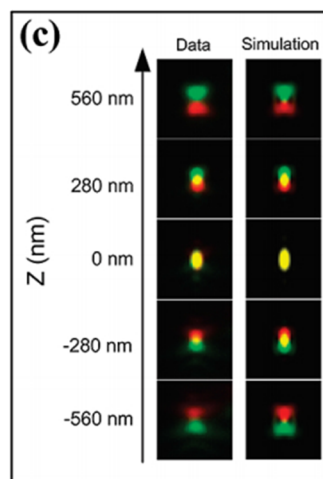
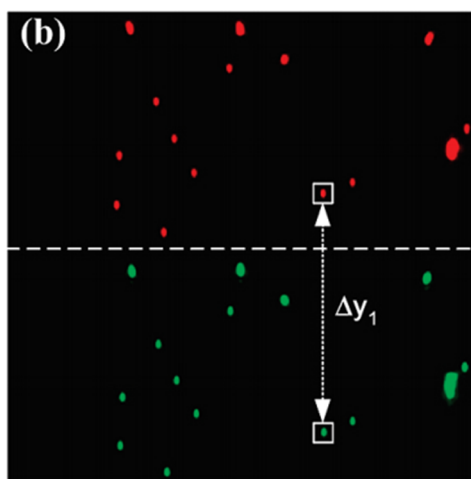


FIG. 7. Schematic of the *parallax* technique and the resultant two-channel disparities. Image adapted with permission from Sun *et al.*, *Nano Lett.* **9**, 2676–2682 (2009). Copyright 2009 American Chemical Society.⁸⁷



emitters, this technique also enables 3D localization from image disparities. These three techniques are all based on splitting the pupil of a conventional microscope and provide a depth range that is similar to that of the conventional DL-PSF; that is, there is no range extension.

Airy beams exhibit self-accelerating translations,^{89,90} which can be used for encoding the depth of particles.^{51,85,86} The diffraction-free propagation of the beam increases the depth over which a particle can be detected with useful SNR, but the spatially extended intensity profile of the Airy PSF introduces difficulty in precise

localization of the PSF and reduces the peak SNR. Jia *et al.* modified the Airy beam using a truncated cubic phase mask, yielding a self-bending PSF (SB-PSF) for 3D localization microscopy⁸⁵ (Fig. 8). The pupil truncation eliminates the side lobes, enabling simple Gaussian functions to be used for centroiding the PSF profile, but at the cost of a 30% reduction in the optical efficiency, which degrades the achievable precision. A further disadvantage is that the PSF acceleration is symmetric about the focal plane, so only half of the diffraction-free range of the PSF (on one side of the focus) can be utilized for depth discrimination.

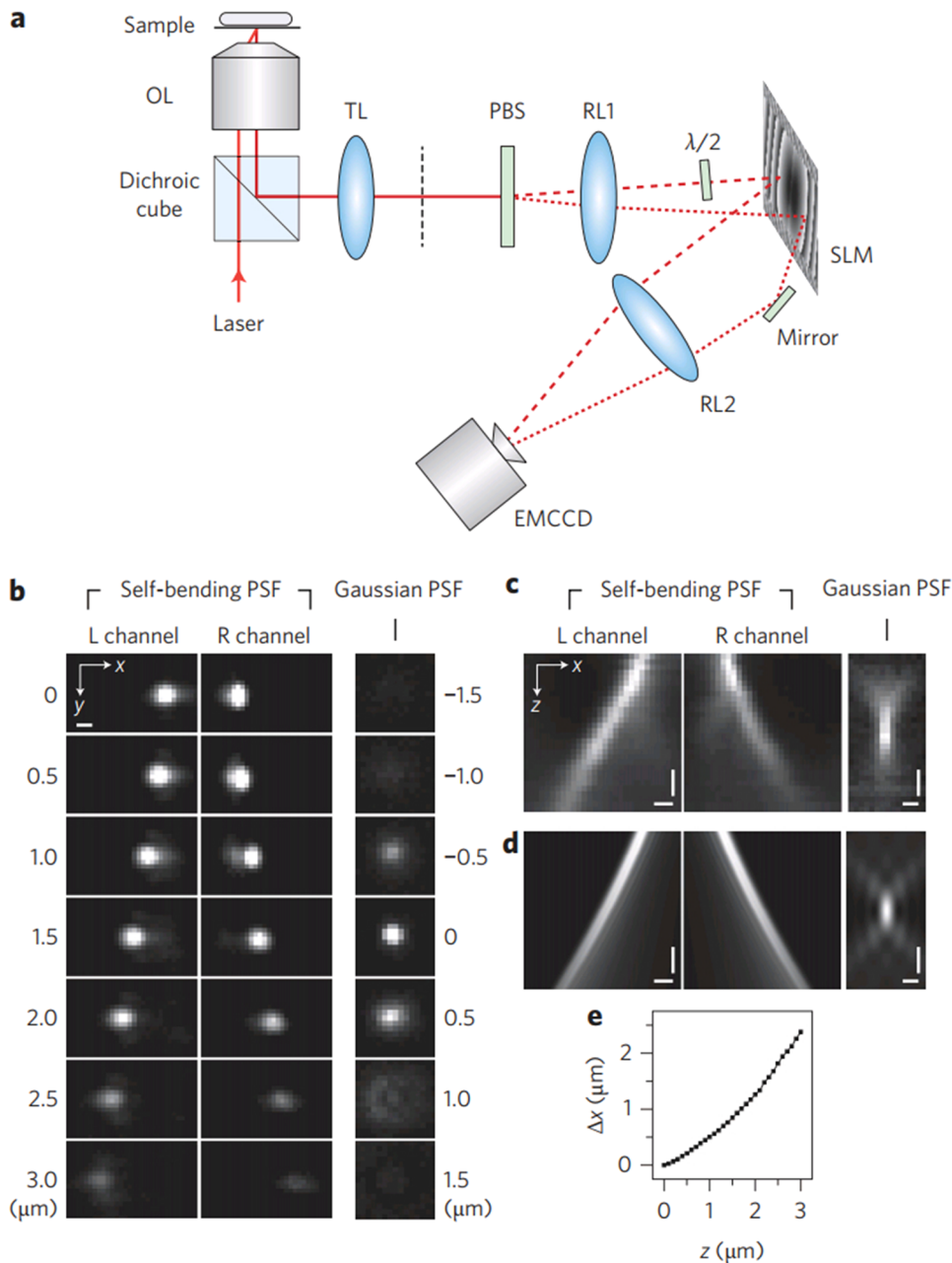


FIG. 8. Self-bending PSF (SB-PSF) and the schematic of its imaging setup, the collected photons are split into two imaging channels and guided onto the two halves of an SLM, respectively. Image adapted with permission from S. Jia, J. C. Vaughan, and X. Zhuang, *Nat. Photonics* **8**, 302–306 (2014). Copyright 2014 Springer Nature.⁸⁵

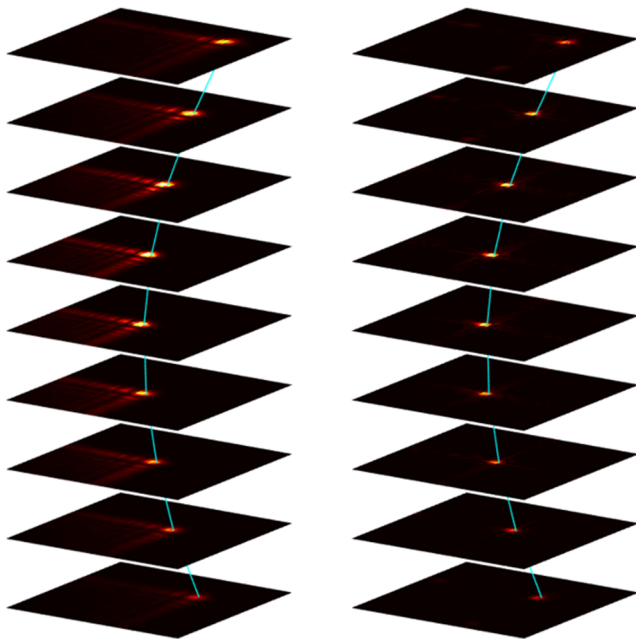


FIG. 9. Airy-beam PSF (AB-PSF) and corresponding deconvolved PSF on a 0.5NA system over a depth range of $100\ \mu\text{m}$. Image adapted from Zhou *et al.*, *Biomed. Opt. Express* 9, 6444 (2018). Copyright 2018 Author(s), licensed under a Creative Commons Attribution 4.0 License.⁸⁶

We have reported the use of an intact Airy-beam PSF (AB-PSF) without pupil truncation.^{51,86} Due to its depth-invariant intensity profile, the AB-PSF can be deconvolved with a single calibration PSF (deconvolution kernel), yielding a spot which exhibits the same lateral translation as the AB-PSF (Fig. 9). To measure the lateral translation of the deconvolved PSF in practice, a biplane setup is used, in which a defocus offset is introduced between two

imaging channels. This defocus offset causes image disparity in the two imaging channels which is a linear function of axial displacement of the source. This technique (termed Airy-CKM) enables the complete diffraction-free range of the AB-PSF on both sides of the nominal focus to be utilized (since the sign of defocus can be inferred) and yields a constant z sensitivity (which is proportional to the defocus offset and the inverse of the phase mask strength⁵¹). Note that Airy-beam-based PSFs tend to have lower peak intensity compared to compact PSFs like the DH-PSF and corkscrew PSF. Although deconvolution restores the apparent peak intensity for the recovered compact PSF, the larger number of pixels used to record the extended PSF adds a higher noise level, tending to reduce the SNR compared to what would be recorded directly for a compact PSF.

4. CRLB optimized PSFs

Fisher information is used in microscopy to quantify the statistical limit on the localization precision that is achievable using a specific PSF. This limit is known at the Cramér-Rao lower bound. Shechtman *et al.* developed an information-optimized PSF family: the tetrapod PSFs.^{91,92} The first 55 Zernike polynomials were used as the basis set for optimization of the pupil function that yields a PSF with the best localization precision (i.e., the lowest CRLB) for a specific depth range. They first reported a saddle-point phase mask for $3\ \mu\text{m}$ depth and a cat mask for a $6\ \mu\text{m}$ range, and then a family of CRLB-optimized PSFs termed tetrapod PSFs were reported as shown in Fig. 10.

A key distinction between the information-optimized PSFs and those described in Subsections II C 2 and II C 3 is that they yield extended PSFs where the depth is encoded, not in simple geometrical transforms (rotation and translation) but instead the depth is encoded in the complex shape of the PSF. To extract the 3D coordinates, a phase-retrieval-based maximum-likelihood estimation (PR-MLE) was utilized.⁹³ A stack of calibration PSFs with known z spacing is first recorded to retrieve the actual pupil function of the

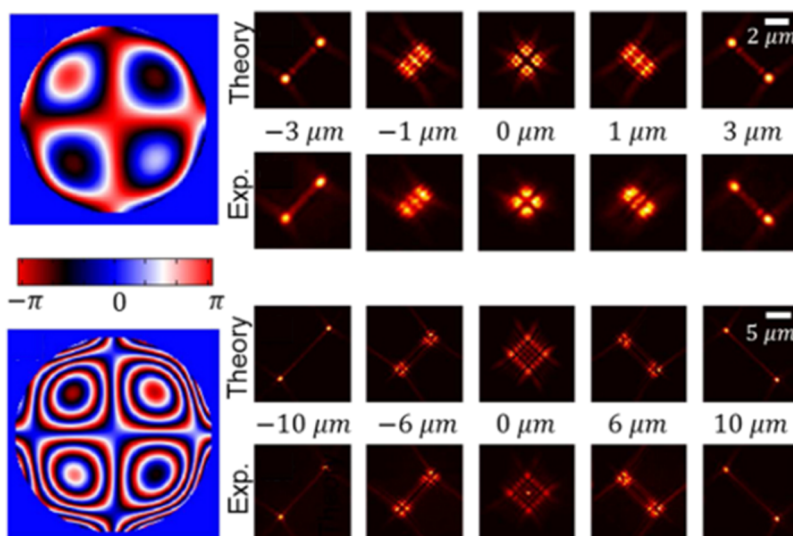


FIG. 10. Tetrapod phase masks and corresponding PSFs, optimized for $6\ \mu\text{m}$ (upper) and $20\ \mu\text{m}$ range (lower). Image adapted with permission from Shechtman *et al.*, *Nano Lett.* 15, 4194–4199 (2015). Copyright 2015 American Chemical Society, further permissions should be directed to the ACS.⁹¹

imaging system, which is then used to generate a model PSF with free parameters (x, y, z coordinates; total number of photons, N_{ph} ; and average number of photons per pixel, N_{bg}). By minimizing the negative likelihood function between the experimentally recorded PSF and the model PSF, one can determine the most probable values of the parameters corresponding to each recorded PSF. It has been shown that MLE can yield a localization precision close to the theoretical CRLB limit;^{92,94} however, the minimization process of the likelihood function is computationally intense, especially if the PSF shape is self-similar and induces many local minima in the optimization process. A disadvantage of the MLE-based estimation algorithm is that overlapping PSFs will inevitably alter the likelihood function and therefore degrade the achievable localization precision. It is possible to compute the joint likelihood for several emitters, but this requires a clustering step and significantly adds to the complexity and computational burden.

III. COMPARISON OF LOCALIZATION PRECISIONS

In this section, we compare the localization precision and the axial range that can be simultaneously achieved, for the various localization techniques. A key component in localization microscopy is the precise and accurate estimation of the 3D particle positions from the 2D image. Several types of estimators can be used, including least-squares fitting and maximum-likelihood estimation, discussed in Sec. IV, which complicates the comparison. For example, when using astigmatism for localization, the ellipticity of the PSF is usually calculated to estimate the 3D location; in rotation-based and translation-based techniques, 2D-Gaussian functions can be fitted to the main lobes to calculate rotation angles and disparities, while the tetrapod PSFs require the use of MLE for 3D localization. Furthermore, for any single technique, different estimators can provide different localization precisions; for example, MLE has been demonstrated to produce better localization precision than least-square fitting under low-background levels.⁹⁴ Thus, to assess and compare localization performance, a metric that is independent of the specific localization estimators is desirable. The CRLB is such a metric because it gives a lower bound on the variance of any unbiased estimators when estimating a parameter. Thus, if the spatial coordinates are parameters to be estimated, the CRLB gives the lowest achievable standard deviation in $x, y,$ and z (i.e., the localization precision). This allows us to perform a direct comparison of localization techniques that is independent of the estimation method used. The PSF model which encodes more information about $x, y,$ and z has better localization precision, regardless of the estimator used for localization.

To characterize the imaging system mathematically, we employ here the ‘‘Poisson model’’ which takes into account the pixelation of the detector, photon shot noise from the object, and from the background fluorescence.¹⁹ This data model assumes that the detector does not introduce significant additional read-out noise. However, it is reasonable and sufficient for comparison purposes and is often used in other CRLB simulations.⁹⁵ With this assumption, the Fisher information matrix can be written as

$$I(\theta) = \sum_{k=1}^K \frac{1}{\mu_{\theta,k} + \beta_{\theta,k}} \left(\frac{\partial \ln \mu_{\theta,k}}{\partial \theta} \right)^T \left(\frac{\partial \ln \mu_{\theta,k}}{\partial \theta} \right), \quad (4)$$

where $\theta = (x, y, z)$ are the coordinates to be estimated. $\mu_{\theta,k}$ is the expected count of signal photons for the k th pixel and $\beta_{\theta,k}$ is the expected count of background photons. $\mu_{\theta,k}$ can be derived given the PSF model and the total number of detected photons. For pupil-engineered techniques, a corresponding phase or amplitude is added to the pupil function $P(k_x, k_y)$ [Eq. (3)], as depicted in Fig. 11, to yield the associated PSF. From the Cramer-Rao inequality, the variance of θ is bounded by the inverse of the diagonal element. Thus, the best achievable precision of parameter θ_i is given by

$$CRLB_{\theta_i} = \sqrt{I_{ii}^{-1}(\theta)}. \quad (5)$$

We have conducted simulations to calculate the CRLB as follows. We assume a 100x, 1.45NA oil-immersion objective, with an oil refractive index of $n = 1.515$ and a detector with a $16 \mu\text{m}$ pixel pitch. We assume 4000 photons enter the objective aperture for each localization, at an emission wavelength of 650 nm, and a background of 10 photons per pixel at the detector. This approximates state-of-the-art measurement for typical low-photon, single-molecule experiments, using, for example, the *Alexa Fluor 647* dye.

Figure 11(a) shows the CRLBs for a conventional microscope, i.e., a diffraction-limited system. As expected, it yields the best CRLBs in x and y for in-focus imaging due to the highly concentrated DL-PSF. As defocus increases however, the achievable precision in x and y degrades rapidly due to the expanding PSF and associated reduction in SNR. In contrast, the DL-PSF has zero depth-sensitivity near the focal plane, yielding a very poor CRLB for z . Additionally, the DL-PSF is symmetric above and below the focus, making it difficult to assign an unambiguous z coordinate to the point source. All these aspects clearly demonstrate that the DL-PSF is ideal for 2D localization, but is not suitable for 3D applications.

The use of an astigmatic PSF can improve the z sensitivity near the focal plane and can break the sign ambiguity associated with the DL-PSF. In our simulation, quadratic phases with opposite signs in the x and y directions were added to the pupil function, with a $0.8 \mu\text{m}$ difference in the tangential and sagittal focal planes. This breaks the symmetry in the x and y CRLBs as shown in Fig. 11(b). The best CRLB occurs at the focal plane of the corresponding direction. However, the z CRLB deteriorates at the two focal planes due to the lack of depth sensitivity. Astigmatism yields CRLBs better than 10 nm in xyz over a depth range of about $1.2 \mu\text{m}$, which is double that achievable using the DL-PSF.

To test the biplane technique, we equally divided the total number of photons between two DL-PSFs with a $0.5 \mu\text{m}$ difference in their focal planes. The CRLBs were then calculated by concatenating the two images, or adding their corresponding Fisher-information matrix together, with the assumption that the total information is the summation of the information from both channels. From Fig. 11(c), it is clear that the biplane technique produces better CRLBs than the conventional and astigmatic PSFs. The CRLBs in x and y do not exhibit the displacement as in Fig. 11(b), and they plateau near the nominal focal plane. The z CRLB, however, behaves similarly to that of astigmatism, as it gets worse near the two focal planes. The biplane technique yields CRLBs better than 10 nm in all dimensions over a depth range of nearly $1.7 \mu\text{m}$ which is about three times the useful range of a conventional single-focal-plane system.

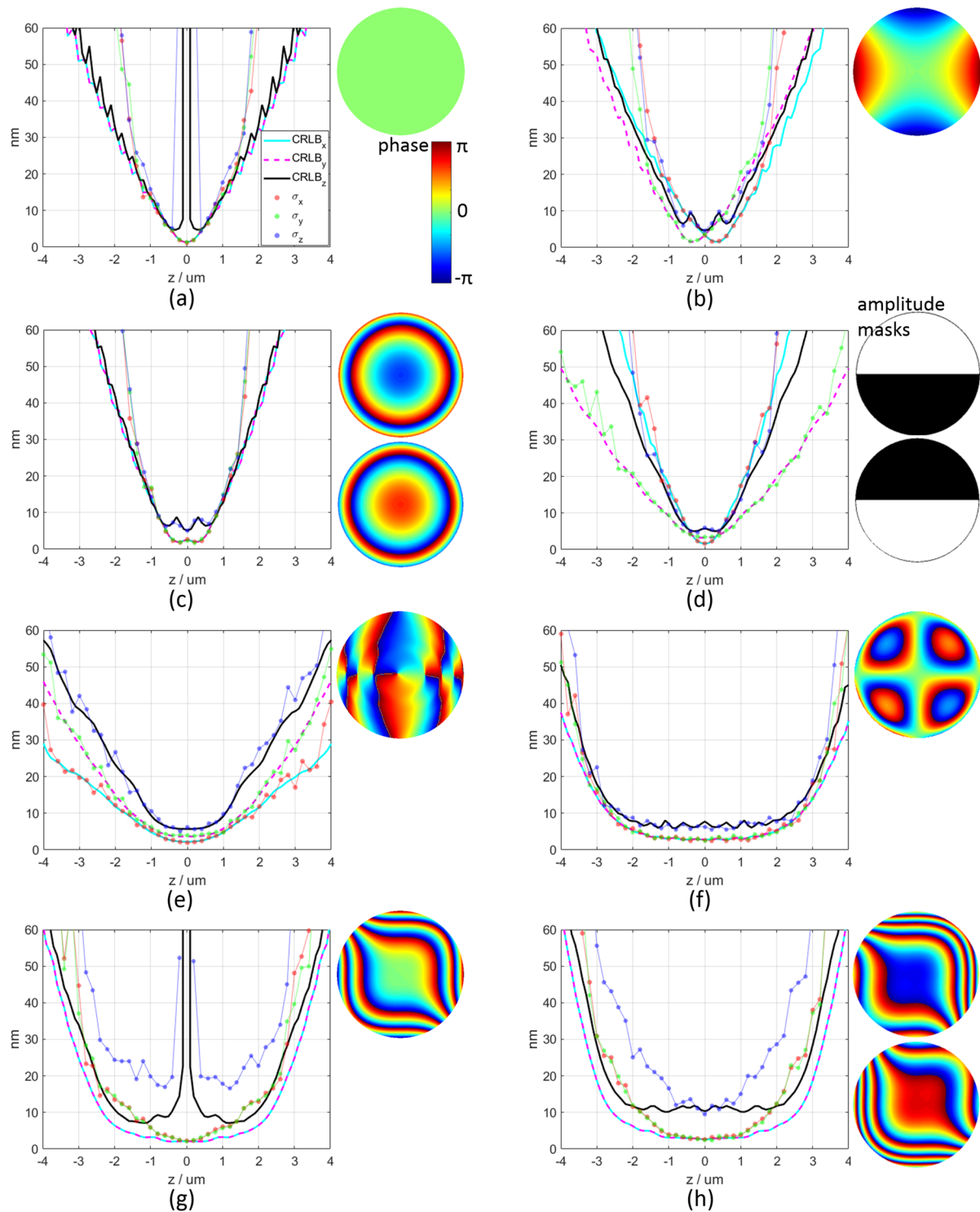


FIG. 11. Cramér-Rao lower bound (CRLB) and the localization precision from maximum-likelihood estimation (σ_x , σ_y , σ_z) for (a) conventional DL-PSF, (b) astigmatic-PSF, (c) bi-plane technique, (d) *parallax* technique, (e) DH-PSF, (f) tetrapod PSF, (g) Airy-beam PSF, and (h) bi-plane Airy-beam PSF. We assume 4000 photons per localization and an average of background of 10 photons per pixel. The corresponding phase or amplitude masks used are also shown next to the graphs, where the phase profiles shown are wrapped to $(-\pi, \pi)$.

The *parallax* technique is based on the DL-PSF but splits the pupil into two halves, effectively creating two “side views.” To simulate this, we generated PSFs for the two “side views” individually by placing an amplitude mask that is “half one, half zero” as shown in Fig. 11(d). Similar to the biplane treatment, half the photons were used for each channel and the images were concatenated to calculate the CRLBs. This technique also yields a better performance than the conventional and astigmatic systems. It has good z sensitivity near the focal plane and does not exhibit the “M-shaped” z precision as in the astigmatism and biplane methods. Interestingly, the y CRLB is better than that in the x direction at large defocus. This is because the effective NA is lower in the y direction as the pupil is cropped to create the two channels, resulting in a larger DOF. The *parallax* technique yields CRLBs better than 10 nm over an axial range of about $1.3 \mu\text{m}$.

To calculate the CRLBs for the DH-PSF, we performed an iterative simulation as described by Pavani and Piestun.⁸¹ The phase mask obtained from this, and its corresponding CRLBs are shown in Fig. 11(e). The DH-PSF yields better performance in terms of both the depth range and the precision, compared to the above discussed techniques. The fact that most of the photons are concentrated in the two rotating lobes yields a high SNR and, therefore, a good localization precision. Due to its continuous rotation, the DH-PSF has a constant z sensitivity over an axial range of about $1.8 \mu\text{m}$. Note that the operable range of the DH-PSF is limited by both the achievable precision and the 180° rotation. In this case, about $2.6 \mu\text{m}$ can be utilized without ambiguity.

An analysis for the tetrapod PSF was also performed based on the optimization process described in Refs. 91 and 92. A tetrapod mask optimized for $4 \mu\text{m}$ and the calculated CRLBs as shown in Fig. 11(f). Because the tetrapod PSF is optimized against the mean CRLB, it therefore displays the best mean CRLBs in all directions. As can be observed in Fig. 11(f), the CRLBs are flat between -2 and $2 \mu\text{m}$, and are lower than 10 nm in all dimensions over a depth range of about $4.8 \mu\text{m}$. This exceeds all of the above discussed techniques, making the tetrapod PSF a preferred tool for imaging over an extended depth range and through thick samples. However, the tetrapod PSF is a “shape-based” PSF and requires PR-MLE for the data analysis, which is time consuming, especially when global minimization is used to avoid the local minima in the likelihood function. Additionally, the likelihood function can be altered in the case of overlapping PSFs, degrading the localization precision. This may, in practice, lead to a worse achievable precision when using the tetrapod PSF.

Lastly, we calculated the CRLBs for the AB-PSF and bi-plane AB-PSF. A cubic phase with $\alpha = 2.5$ was added to the pupil function, which yields the CRLBs as shown in Fig. 11(g). The diffraction-free propagation improves SNR at large levels of defocus, as can be seen from the x and y CRLBs which stay below 10 nm for around a $4.6 \mu\text{m}$ depth range. The parabolic z -dependent lateral translation helps to maintain good depth sensitivity at large defocus. However, there are also obvious disadvantages: (1) the CRLB in z shows zero depth-sensitivity near the focal plane as in the DL-PSF. (2) A sign ambiguity in z exists, as the AB-PSF translates symmetrically above and below the focal plane. Nevertheless, the AB-PSF still gives about $1.5 \mu\text{m}$ depth range on one side of the focal plane, over which the CRLBs are better than 10 nm in all dimensions. The Airy-CKM method^{51,86} combines the AB-PSF and bi-plane imaging to help eliminate the z

insensitivity near the focal plane. With a $1.2 \mu\text{m}$ separation between focal planes, Airy-CKM yields the CRLBs shown in Fig. 11(h). Compared to the conventional bi-plane technique with a DL-PSF, the AB-PSF greatly extends the depth range. The CRLBs are relatively uniform in all dimensions over a depth range of about $4 \mu\text{m}$, and are better than 12 nm. The precision in Fig. 11(h) can be improved by using a weaker cubic phase modulation at the cost of a reduced overall depth range.

In addition to the CRLBs, we also calculated the precision from a maximum-likelihood estimation of each of the techniques compared in this section. MLE is a universal estimator that can be used for any PSF with xyz -dependence. The same parameters were used to generate the PSFs as in the CRLB calculations, and the MATLAB optimizer (*fmincon* as used in Refs. 91 and 92) was used to find the set of parameters that yields the maximum likelihood function. Again, only Poisson noise is considered here and the precision shown in Fig. 11 is the standard deviation from 100 repeated measurements. Our simulations show that MLE approaches the CRLB, and it furthermore approaches the CRLBs only in the regions where the PSF exhibits good SNR as shown in Fig. 11. These results are in agreement with previous publications.^{92,94} Our simulation also shows that MLE falls easily into local minima (of the negative likelihood function⁹²) when used with PSFs that have periodic structures in their intensity profile, e.g., the AB-PSF (as shown in Fig. 8) and the in-focus region of the tetrapod PSF (as shown in Fig. 10). Global minimization can minimize the occurrence of local minima but is time consuming. Note that the MLE results in Figs. 11(f) and 11(g) were obtained using global optimization with multistarting points.

IV. PRACTICAL ESTIMATORS FOR POINT SOURCE LOCALIZATION

With all the aforementioned techniques, a reliable estimator is required to infer the 3D position of a particle from its PSF. As mentioned above, this can be as simple as measuring the radius of the Airy disk, but such an approach tends to have poor precision. In this section, we will discuss several popular methods for practical estimation and explain the advantages and disadvantages of each.

There are three major categories of algorithm for point source estimation: least-squares (LS) fitting, maximum-likelihood estimation (MLE), and compressed sensing (CS). Briefly, LS is the simplest and fastest approach, but is limited in its application to 3D localization; MLE is very precise, but slow to converge on a solution; and CS can cope with very high density images, but is slow and very memory intensive. Detailed comparisons of these techniques can be found in Cheezum *et al.*,⁹⁶ Abraham *et al.*,⁹⁴ and Small and Stahlheber.¹⁷ A discussion of each technique will follow.

A. Least-squares fitting

Given a PSF model, $\mu_k(\theta)$, and some pixelated image data, q_k , the method of least squares seeks to minimize the sum of the square errors between the image and model over the model parameters, θ

$$\arg \min_{\theta \in \Theta} \sum_{k=1}^K (q_k - \mu_k(\theta))^2. \quad (6)$$

Practically, this can be achieved using nonlinear fitting with algorithms such as Levenberg-Marquardt.⁹⁷

LS is very commonly used for 2D point localization, by approximating the central lobe of the Airy disk with a 2D Gaussian function,

$$\mu(\theta) = N \exp\left(\frac{(x-x_0)^2}{\sigma_x} + \frac{(y-y_0)^2}{\sigma_y}\right) + \beta, \quad (7)$$

whose mean values (x_0, y_0) are the estimated particle coordinates, and N and β are the signal and background photon counts, respectively. Gaussian estimation can approach the CRLB for localizing emitters in 2D, but the model cannot be extended to account for 3D PSF behavior, which requires more accurate models of the image-forming process. Given knowledge of the pupil function, $P(k_x, k_y)$, a model can be derived from Eq. (3). For example, in the case of an Airy disk, the pupil is just a binary function over the aperture. Using this type of model requires reliable estimates of the microscope experimental parameters (e.g., NA, M , λ), such that the model accurately approximates experimental behavior. If there is some mismatch between model and experiment, results from the localization algorithm will be biased.

B. Maximum likelihood estimation

Maximum likelihood estimation was first demonstrated for point localization by Auget *et al.*,⁹⁸ who showed that it could precisely predict the axial position of a particle from the shape of the Airy disk. Like least-squares fitting, MLE requires a suitable model of the PSF, but instead of finding the minimum least-squares error between the image and model prediction, it finds the model parameters which maximize the log-likelihood between the two.

Given a PSF model, $\mu(\theta)$, dependent on the parameter set $\theta = \{x, y, z, N, \beta\}$, where (x, y, z) is the emitter spatial coordinates, N is the number of photons emitted, and β is a constant background, let the expected photon count in pixel k be written as $\mu_{\theta,k}$. The Poisson-distributed probability of observing q_k photons in pixel k is therefore

$$P(q_k) = \frac{e^{-\mu_{\theta,k}} \mu_{\theta,k}^{q_k}}{q_k!}. \quad (8)$$

The probability that an image, Q , is measured is therefore the joint probability over every pixel $P(Q = \{q_1 \dots q_K\}) = \prod_{k=1}^K P(q_k)$.

This means that given a measurement of an image, Q , the log-likelihood of the model values, $\mu(\theta)$, that give rise to such measurement is

$$\begin{aligned} \ell(\mu_\theta|Q) &= \log\left(\prod_{k=1}^K P(q_k)\right) \\ &= \sum_{k=1}^K [q_k \log(\mu_{\theta,k}) - \mu_{\theta,k} - \log(q_k!)]. \end{aligned} \quad (9)$$

Maximizing the log-likelihood, $\ell(\mu_\theta)$ therefore gives the best statistical estimate of the parameters θ (i.e., the emitter coordinates) that result in the measurement of the image Q . Practically, this is an optimization procedure in which the PSF model is compared against the measured image over successive parameter values, θ . For this purpose, the $\log(q_k!)$ term can be ignored since it does not change with θ .

A natural extension of the MLE concept is maximum *a posteriori* (MAP) estimation, which incorporates prior probabilities. Lindén *et al.*⁹⁹ have shown that by including some physical constraints on the likelihood function, such as excluding PSFs that are smaller than the diffraction limit and asserting an exponentially decaying probability for large PSFs, they can achieve better than CRLB localization precision.

C. Compressed sensing

Localization by compressed sensing takes a fundamentally different approach from the statistical estimation of LS and MLE. There are two varieties: convex optimization (CO) and matching pursuit (MP).

In CO,¹⁰⁰ we consider that the set of point emitters, x , within their 3D volume is downsampled and projected onto the image, q , by a function, A , representing the PSF. Under the assumption that x is sparse, the emitters can therefore be localized by minimizing the L_1 norm (i.e., number of elements) of x such that $q = Ax$. Practically, this can be written as

$$\min \|x\|_1 \quad s.t. \quad \|q - Ax\|_2 < \varepsilon, \quad (10)$$

where $\|x\|_1$ is the L_1 norm of x , $\|q - Ax\|_2$ is the L_2 norm of the difference between the image and estimation (i.e., sum of square errors) and ε is a small number. With this constraint, CO converges on the

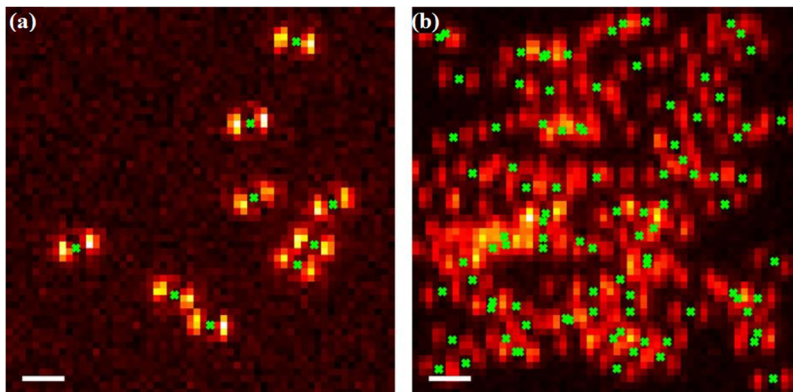


FIG. 12. Typical maximum densities of least squares (a) and compressed sensing localization algorithms with a DH-PSF. Image adapted from A. Barsic, G. Grover, and R. Piestun, *Sci. Rep.* **4**, 5388 (2014). Copyright 2014 Author(s), licensed under a Creative Commons Attribution 4.0 License.¹⁰⁶

solution of least emitters which reproduce the image after projection by the function A .

Matching pursuit algorithms operate by iteratively subtracting each localized model PSF from the image until they cannot find anymore. DAOSTORM^{101,102} and deconSTORM¹⁰³ are examples of this.

Normally, LS and MLE algorithms fit a single PSF to each of the identified points. In cases where PSFs overlap, this can produce errors in localization or even false positives. Multiple PSF estimation is a possibility, but this requires prior knowledge of the number of overlapping points.^{101,104} CS makes no such assumptions and has therefore been demonstrated to work with very high-density images.^{105–108} Figure 12 shows a comparison between typical maximum densities of LS and CS algorithms when used with the DH-PSF.¹⁰⁶

V. CONCLUSION AND PERSPECTIVE

The importance of point localization microscopy arises from its ability to enable fundamental advances in fields ranging from biomedicine (e.g., single-molecule imaging) to physics and engineering (e.g., fluid-flow mapping, sensing with nanoparticles). This rapidly expanding field is reported in about 3000 articles per year according to *Scopus*. In particular, 3D-imaging techniques using high-NA objectives are capturing increasing attention, especially in pupil engineering, which allows researchers to design and optimize specific properties of the PSF, such as shape, rotation, or translation. We expect further advances in pupil-engineering techniques and believe that as this technology matures, many more interesting developments will continue to push the achievable limits of localization precision, DOF, and particle density. The techniques discussed in this article have enabled precise point localization in all three dimensions and in an extended axial region, with a localization precision comparable to that which can be achieved in 2D.

We have reviewed and compared the most important 3D imaging techniques for localization microscopy, in terms of localization precision and depth range. Their CRLBs were calculated as a gold-standard figure of merit. While the conventional DL-PSF, astigmatic PSF, biplane technique, and *parallax* technique yield a narrower depth range than the rest, they each offer specific advantages in terms of simple implementation or commercial availability. Thus, we expect each technique to continue to play an important role in this field, especially for applications where the sample or the volume of interest is relatively shallow. On the other hand, DH-PSF, corkscrew PSF, SB-PSF, Airy-CKM, tetrapod PSF yield extended axial ranges with high localization precision and are suitable for imaging thick samples. The DH-PSF has a relatively small depth range but is more robust at lower SNRs. The Airy-CKM technique and the tetrapod PSF have the largest depth range but they have their own drawbacks: Airy-CKM has a lower precision than the tetrapod and requires biplane imaging to deduce the z coordinate, while the tetrapod mask is nonanalytical and the 3D coordinates are encoded in the shape of the tetrapod PSF and so requires computationally expensive MLE algorithms for the localization. This can yield degraded precision if PSFs overlap. Therefore, we look forward to improved techniques to be reported on these two directions.

TABLE I. Comparison of currently available techniques for 3D localization microscopy.

| Techniques | Implementation | Continuous mask or not | Analytical mask or not | Commercial availability | Example application | Comments |
|-------------------------------|------------------------------|------------------------|------------------------|-------------------------|---|--|
| DL-PSF | Conventional microscope | ... | Yes | Yes | Particle image velocimetry | ... |
| Astigmatism ⁷⁷ | Cylindrical lens | Yes | Yes | Yes | Single molecule microscopy ⁷³ | ... |
| MUM ³⁶ | Multiple cameras | ... | Yes | No | Study of fast intracellular dynamics in live cells ³⁶ | Multiple cameras |
| Parallax ⁸⁷ | Split pupil by mirror | ... | ... | ... | 3D tracking of vesicles in living adipocytes ⁸⁷ | ... |
| Wedge prism ⁸⁸ | Split pupil by wedge prism | ... | ... | ... | Observation of quantum dot bound to a sliding microtubule ⁸⁸ | Modification inside microscope |
| DH-PSF ^{78,81} | 4f with DH mask | No | No | No | 3D super-resolution | 180° rotation limit |
| DH-PSF-S ⁸³ | 4f with SPINDLE mask | No | Yes | Yes | Super-resolution imaging | 180° rotation limit |
| Corkscrew PSF ⁷⁹ | 4f with corkscrew mask | No | No | Yes | Image of beads on a PDMS grating | Sequential images needed for deducing z |
| SB-PSF ⁸⁵ | 4f with truncated cubic mask | No | Yes | No | Super-resolution imaging | Additional photon loss from truncated pupil |
| Airy-CKM ^{51,86} | 4f with cubic mask | Yes | Yes | No | <i>in vivo</i> blood-flow mapping | Lower peak signal |
| Tetrapod PSF ^{91,92} | 4f with tetrapod mask | Yes | No | Yes | 3D flow measurement | Degrade precision at low SNR and with overlapping PSFs |

There are additional considerations when choosing between these techniques, such as the complexity of implementation, the photon-efficiency of the phase mask, the commercial availability of components and systems, and the cost. Some of these aspects are listed in Table I, in which we also consider whether a phase mask can be described by an analytical function on the pupil, which influences both the flexibility for adjusting modulation strength and for its fabrication. Similarly, whether a mask exhibits a continuous surface is also important for its fabrication, as phase profiles with 2π jumps that cannot be unwrapped are not ideal for manufacturing and may also cause some additional photon loss due to scattering. A continuous phase profile is also required for implementation of a phase mask using a deformable mirror (which is preferred over SLMs due to their higher photon efficiency).

There has also recently been consideration of the extension of point localization precision beyond the classical limit of the CRLB. One approach involves deriving the Fisher information in terms of the quantum statistics of the emitter wave function, resulting in a localization precision limit which can be a factor of $\sqrt{2}$ smaller than what can be achieved in classically. It has been suggested that interferometric methods can approach this quantum bound.¹⁰⁹ Tsang *et al.*¹¹⁰ showed that quantum treatment allows localization of two overlapping point sources without a reduction in precision. Another approach to achieving improved precision is to exploit prior knowledge: Lindén *et al.* extended MAP to MLE⁹⁹ including physical constraints on the likelihood function, such as excluding subdiffraction limit sized PSFs and an exponentially decaying probability of large PSFs, to achieve localization precision below the CRLB. This suggests there is room for more sophisticated prior probabilities to be used, which have not been explored yet.

Besides the extension in the depth range and isotropic localization precision, recent developments also suggest a trend for localizing emitters from images with ever higher densities of points, which is underlined by the need in super-resolution microscopy to perform image reconstructions using fewer frames, i.e., with faster acquisition process. Also, extending localization microscopy to thicker sample ranges increases the density of points projected onto the detector plane. Localization with compressed sensing has automated a large part of the traditional particle-identification and localization processes. The recent publication of sophisticated algorithms such as TVSTORM¹⁰⁸ and hybrid CO-MP algorithms¹⁰² suggests a rich opportunity for refining CS even further. There may even be some possibilities for the development of deep-learning algorithms based on compressed sensing. It is noteworthy that Wiener deconvolution of the AB-PSF was reported in the Airy-CKM technique to yield compact PSF lobes,⁵¹ which has potential for imaging high tracer densities with comparably fast and simple processing. We look forward to further explorations of deconvolution-based algorithms in this field.

ACKNOWLEDGMENTS

The authors acknowledge financial support from the Engineering and Physical Sciences Research Council (Grant No. EP/L016753/1), the Leverhulme Trust (Grant No. ECF-2016-757), and the China Scholarship Council (Grant No. 201503170229).

REFERENCES

- G. J. Schütz, G. Kada, V. P. Pastushenko, and H. Schindler, "Properties of lipid microdomains in a muscle cell membrane visualized by single molecule microscopy," *EMBO J.* **19**, 892–901 (2000).
- A. D. Douglass and R. D. Vale, "Single-molecule microscopy reveals plasma membrane microdomains created by protein-protein networks that exclude or trap signaling molecules in t cells," *Cell* **121**, 937–950 (2005).
- M. J. Rust, M. Bates, and X. Zhuang, "Sub-diffraction-limit imaging by stochastic optical reconstruction microscopy (storm)," *Nat. Methods* **3**, 793–796 (2006).
- E. Betzig, G. H. Patterson, R. Sougrat, O. W. Lindwasser, S. Olenych, J. S. Bonifacino, M. W. Davidson, J. Lippincott-Schwartz, and H. F. Hess, "Imaging intracellular fluorescent proteins at nanometer resolution," *Science* **313**, 1642–1645 (2006).
- J. Ries, C. Kaplan, E. Platonova, H. Eghlidi, and H. Ewers, "A simple, versatile method for GFP-based super-resolution microscopy via nanobodies," *Nat. Methods* **9**, 582 (2012).
- D. R. Larson, W. R. Zipfel, R. M. Williams, S. W. Clark, M. P. Bruchez, F. W. Wise, and W. W. Webb, "Water-soluble quantum dots for multiphoton fluorescence imaging *in vivo*," *Science* **300**, 1434–1436 (2003).
- Y. Geng, P. Dalhaimer, S. Cai, R. Tsai, M. Tewari, T. Minko, and D. E. Discher, "Shape effects of filaments versus spherical particles in flow and drug delivery," *Nat. Nanotechnol.* **2**, 249 (2007).
- R. Lima, S. Wada, S. Tanaka, M. Takeda, T. Ishikawa, K.-i. Tsubota, Y. Imai, and T. Yamaguchi, "In vitro blood flow in a rectangular PDMS microchannel: Experimental observations using a confocal micro-PIV system," *Biomed. Microdevices* **10**, 153–167 (2008).
- W. R. Legant, J. S. Miller, B. L. Blakely, D. M. Cohen, G. M. Genin, and C. S. Chen, "Measurement of mechanical tractions exerted by cells in three-dimensional matrices," *Nat. Methods* **7**, 969–971 (2010).
- S. Khetan, M. Guvendiren, W. R. Legant, D. M. Cohen, C. S. Chen, and J. A. Burdick, "Degradation-mediated cellular traction directs stem cell fate in covalently crosslinked three-dimensional hydrogels," *Nat. Mater.* **12**, 458 (2013).
- J. Westerweel, "Fundamentals of digital particle image velocimetry," *Meas. Sci. Technol.* **8**, 1379 (1997).
- A. K. Singh, E. B. Cummings, and D. J. Throckmorton, "Fluorescent liposome flow markers for microscale particle-image velocimetry," *Anal. Chem.* **73**, 1057–1061 (2001).
- R. Lindken, M. Rossi, S. Große, and J. Westerweel, "Micro-particle image velocimetry (μ PIV): Recent developments, applications, and guidelines," *Lab Chip* **9**, 2551–2567 (2009).
- A. von Diezmann, Y. Shechtman, and W. Moerner, "Three-dimensional localization of single molecules for super-resolution imaging and single-particle tracking," *Chem. Rev.* **117**, 7244–7275 (2017).
- H. Shen, L. J. Tauzin, R. Baiyasi, W. Wang, N. Moringo, B. Shuang, and C. F. Landes, "Single particle tracking: From theory to biophysical applications," *Chem. Rev.* **117**, 7331–7376 (2017).
- C. Manzo and M. F. Garcia-Parajo, "A review of progress in single particle tracking: From methods to biophysical insights," *Rep. Prog. Phys.* **78**, 124601 (2015).
- A. Small and S. Stahlheber, "Fluorophore localization algorithms for super-resolution microscopy," *Nat. Methods* **11**, 267 (2014).
- H. Deschout, F. C. Zanacchi, M. Mlodzianoski, A. Diaspro, J. Bewersdorf, S. T. Hess, and K. Braeckmans, "Precisely and accurately localizing single emitters in fluorescence microscopy," *Nat. Methods* **11**, 253 (2014).
- J. Chao, E. S. Ward, and R. J. Ober, "Fisher information theory for parameter estimation in single molecule microscopy: Tutorial," *J. Opt. Soc. Am. A* **33**, B36–B57 (2016).
- L. La Spada and L. Vegni, "Electromagnetic nanoparticles for sensing and medical diagnostic applications," *Materials* **11**, 603–621 (2018).
- V. A. Troutman and J. O. Dabiri, "Single-camera three-dimensional tracking of natural particulate and zooplankton," *Meas. Sci. Technol.* **29**, 075401 (2018).
- D. B. Conkey, R. P. Trivedi, S. R. P. Pavani, I. I. Smalyukh, and R. Piestun, "Three-dimensional parallel particle manipulation and tracking by integrating

- holographic optical tweezers and engineered point spread functions,” *Opt. Express* **19**, 3835–3842 (2011).
- ²³J.-A. Conchello and J. W. Lichtman, “Optical sectioning microscopy,” *Nat. Methods* **2**, 920 (2005).
- ²⁴M. D. Lew, M. P. Backlund, and W. Moerner, “Rotational mobility of single molecules affects localization accuracy in super-resolution fluorescence microscopy,” *Nano Lett.* **13**, 3967–3972 (2013).
- ²⁵M. Speidel, A. Jonáš, and E.-L. Florin, “Three-dimensional tracking of fluorescent nanoparticles with subnanometer precision by use of off-focus imaging,” *Opt. Lett.* **28**, 69–71 (2003).
- ²⁶M. Wu, J. W. Roberts, and M. Buckley, “Three-dimensional fluorescent particle tracking at micron-scale using a single camera,” *Exp. Fluids* **38**, 461–465 (2005).
- ²⁷J. Park and K. Kihm, “Three-dimensional micro-PTV using deconvolution microscopy,” *Exp. Fluids* **40**, 491 (2006).
- ²⁸Z. Zhang and C.-H. Menq, “Three-dimensional particle tracking with subnanometer resolution using off-focus images,” *Appl. Opt.* **47**, 2361–2370 (2008).
- ²⁹L. Gardini, M. Calamai, H. Hatakeyama, M. Kanzaki, M. Capitanio, and F. S. Pavone, “Three-dimensional tracking of quantum dot-conjugated molecules in living cells,” in *Nanoscale Imaging* (Springer, 2018), pp. 425–448.
- ³⁰H. Kirshner, F. Aguet, D. Sage, and M. Unser, “3-d PSF fitting for fluorescence microscopy: Implementation and localization application,” *J. Microsc.* **249**, 13–25 (2013).
- ³¹B. M. Hanser, M. G. L. Gustafsson, D. A. Agard, and J. W. Sedat, “Phase retrieval for high-numerical-aperture optical systems,” *Opt. Lett.* **28**, 801–803 (2003).
- ³²S. F. Gibson and F. Lanni, “Experimental test of an analytical model of aberration in an oil-immersion objective lens used in three-dimensional light microscopy,” *J. Opt. Soc. Am. A* **9**, 154–166 (1992).
- ³³S. Ram, E. S. Ward, R. J. Ober, and P. Prabhath, “Simultaneous imaging of different focal planes in fluorescence microscopy for the study of cellular dynamics in three dimensions,” *IEEE Trans. Nanobioscience* **3**, 237–242 (2004).
- ³⁴S. Ram, J. Chao, P. Prabhath, E. S. Ward, and R. J. Ober, “A novel approach to determining the three-dimensional location of microscopic objects with applications to 3d particle tracking,” *Proc. SPIE* **6443**, 64430D-1–64430D-7 (2007).
- ³⁵R. Velmurugan, J. Chao, S. Ram, E. S. Ward, and R. J. Ober, “Intensity-based axial localization approaches for multifocal plane microscopy,” *Opt. Express* **25**, 3394–3410 (2017).
- ³⁶S. Ram, P. Prabhath, J. Chao, E. S. Ward, and R. J. Ober, “High accuracy 3d quantum dot tracking with multifocal plane microscopy for the study of fast intracellular dynamics in live cells,” *Biophys. J.* **95**, 6025–6043 (2008).
- ³⁷S. Ram, P. Prabhath, E. S. Ward, and R. J. Ober, “Improved single particle localization accuracy with dual objective multifocal plane microscopy,” *Opt. Express* **17**, 6881–6898 (2009).
- ³⁸A. Tahmasbi, S. Ram, J. Chao, A. V. Abraham, F. W. Tang, E. S. Ward, and R. J. Ober, “Designing the focal plane spacing for multifocal plane microscopy,” *Opt. Express* **22**, 16706–16721 (2014).
- ³⁹S. Hell and E. H. Stelzer, “Properties of a 4pi confocal fluorescence microscope,” *J. Opt. Soc. Am. A* **9**, 2159–2166 (1992).
- ⁴⁰P. A. Dalgarno, H. I. Dalgarno, A. Putoud, R. Lambert, L. Paterson, D. C. Logan, D. P. Towers, R. J. Warburton, and A. H. Greenaway, “Multiplane imaging and three dimensional nanoscale particle tracking in biological microscopy,” *Opt. Express* **18**, 877–884 (2010).
- ⁴¹S. Abrahamsson, J. Chen, B. Hajj, S. Stallinga, A. Y. Katsov, J. Wisniewski, G. Mizuguchi, P. Soule, F. Mueller, C. D. Darzacq *et al.*, “Fast multicolor 3d imaging using aberration-corrected multifocus microscopy,” *Nat. Methods* **10**, 60 (2012).
- ⁴²B. Hajj, L. Oudjedi, J.-B. Fiche, M. Dahan, and M. Nollmann, “Highly efficient multicolor multifocus microscopy by optimal design of diffraction binary gratings,” *Sci. Rep.* **7**, 5284 (2017).
- ⁴³K. He, Z. Wang, X. Huang, X. Wang, S. Yoo, P. Ruiz, I. Gdor, A. Selewa, N. J. Ferrier, N. Scherer *et al.*, “Computational multifocal microscopy,” *Biomed. Opt. Express* **9**, 6477–6496 (2018).
- ⁴⁴X. Huang, A. Selewa, X. Wang, M. K. Daddysman, I. Gdor, R. Wilton, A. K. Katsaggelos, O. Cossairt, N. J. Ferrier, M. Hereld *et al.*, “3d snapshot microscopy of extended objects,” preprint [arXiv:1802.01565](https://arxiv.org/abs/1802.01565) (2018).
- ⁴⁵P. Prabhath, Z. Gan, J. Chao, S. Ram, C. Vaccaro, S. Gibbons, R. J. Ober, and E. S. Ward, “Elucidation of intracellular recycling pathways leading to exocytosis of the Fc receptor, FcRn, by using multifocal plane microscopy,” *Proc. Natl. Acad. Sci. U. S. A.* **104**, 5889–5894 (2007).
- ⁴⁶Z. Gan, S. Ram, R. J. Ober, and E. S. Ward, “Using multifocal plane microscopy to reveal novel trafficking processes in the recycling pathway,” *J. Cell Sci.* **126**, 1176 (2013).
- ⁴⁷F. Huang, G. Sirinakis, E. S. Allgeyer, L. K. Schroeder, W. C. Duim, E. B. Kromann, T. Phan, F. E. Rivera-Molina, J. R. Myers, I. Irnov, M. Lessard, Y. Zhang, M. Handel, C. Jacobs-Wagner, C. P. Lusk, J. E. Rothman, D. Toomre, M. J. Booth, and J. Bewersdorf, “Ultra-high resolution 3d imaging of whole cells,” *Cell* **166**, 1028–1040 (2016).
- ⁴⁸B. Hajj, M. El Beheiry, and M. Dahan, “PSF engineering in multifocus microscopy for increased depth volumetric imaging,” *Biomed. Opt. Express* **7**, 726–731 (2016).
- ⁴⁹L. Oudjedi, J.-B. Fiche, S. Abrahamsson, L. Mazenq, A. Lecestre, P.-F. Calmon, A. Cerf, and M. Nöllmann, “Astigmatic multifocus microscopy enables deep 3d super-resolved imaging,” *Biomed. Opt. Express* **7**, 2163–2173 (2016).
- ⁵⁰P. Zammit, A. R. Harvey, and G. Carles, “Extended depth-of-field imaging and ranging in a snapshot,” *Optica* **1**, 209–216 (2014).
- ⁵¹Y. Zhou, P. Zammit, G. Carles, and A. R. Harvey, “Computational localization microscopy with extended axial range,” *Opt. Express* **26**, 7563–7577 (2018).
- ⁵²P. Memmolo, L. Miccio, M. Paturzo, G. D. Caprio, G. Coppola, P. A. Netti, and P. Ferraro, “Recent advances in holographic 3d particle tracking,” *Adv. Opt. Photonics* **7**, 713–755 (2015).
- ⁵³T. Latychevskaia and H.-W. Fink, “Holographic time-resolved particle tracking by means of three-dimensional volumetric deconvolution,” *Opt. Express* **22**, 20994–21003 (2014).
- ⁵⁴S. Murata and N. Yasuda, “Potential of digital holography in particle measurement,” *Opt. Laser Technol.* **32**, 567–574 (2000).
- ⁵⁵G. Pan and H. Meng, “Digital holography of particle fields: Reconstruction by use of complex amplitude,” *Appl. Opt.* **42**, 827–833 (2003).
- ⁵⁶P. Langehanenberg, B. Kemper, D. Dirksen, and G. von Bally, “Autofocusing in digital holographic phase contrast microscopy on pure phase objects for live cell imaging,” *Appl. Opt.* **47**, D176–D182 (2008).
- ⁵⁷F. C. Cheong, B. J. Krishnatreya, and D. G. Grier, “Strategies for three-dimensional particle tracking with holographic video microscopy,” *Opt. Express* **18**, 13563–13573 (2010).
- ⁵⁸D. H. Barnhart, R. J. Adrian, and G. C. Papen, “Phase-conjugate holographic system for high-resolution particle-image velocimetry,” *Appl. Opt.* **33**, 7159–7170 (1994).
- ⁵⁹J. Katz and J. Sheng, “Applications of holography in fluid mechanics and particle dynamics,” *Annu. Rev. Fluid Mech.* **42**, 531–555 (2010).
- ⁶⁰F. Verpillat, F. Joud, P. Desbiolles, and M. Gross, “Dark-field digital holographic microscopy for 3D-tracking of gold nanoparticles,” *Opt. Express* **19**, 26044–26055 (2011).
- ⁶¹N. Warnasooriya, F. Joud, P. Bun, G. Tessier, M. Coppey-Moisan, P. Desbiolles, M. Atlan, M. Abboud, and M. Gross, “Imaging gold nanoparticles in living cell environments using heterodyne digital holographic microscopy,” *Opt. Express* **18**, 3264–3273 (2010).
- ⁶²C. W. McCutchen, “Generalized aperture and the three-dimensional diffraction image,” *J. Opt. Soc. Am.* **54**, 240–244 (1964).
- ⁶³J. Schnitzbauer, R. McGorty, and B. Huang, “4pi fluorescence detection and 3d particle localization with a single objective,” *Opt. Express* **21**, 19701–19708 (2013).
- ⁶⁴A. S. Backer, M. P. Backlund, A. R. von Diezmann, S. J. Sahl, and W. E. Moerner, “A bisected pupil for studying single-molecule orientational dynamics and its application to three-dimensional super-resolution microscopy,” *Appl. Phys. Lett.* **104**, 193701 (2014).
- ⁶⁵C. E. Willert and M. Gharib, “Three-dimensional particle imaging with a single camera,” *Exp. Fluids* **12**, 353–358 (1992).
- ⁶⁶H. Wang and P. Zhao, “Tracking microparticle motions in three-dimensional flow around a microcubic array fabricated on the wall surface,” *Microfluid. Nanofluid.* **22**, 30 (2018).

- ⁶⁷F. Kiebert, J. König, C. Kykal, and H. Schmidt, "Measurements of streams agitated by fluid loaded saw-devices using a volumetric 3-component measurement technique (v3v)," *Phys. Procedia* **70**, 25–29 (2015).
- ⁶⁸L. Kajitani and D. Dabiri, "A full three-dimensional characterization of defocusing digital particle image velocimetry," *Meas. Sci. Technol.* **16**, 790 (2005).
- ⁶⁹C. Cierpka and C. J. Kähler, "Particle imaging techniques for volumetric three-component (3d3c) velocity measurements in microfluidics," *J. Visualization* **15**, 1–31 (2012).
- ⁷⁰C.-H. Lien, C.-Y. Lin, S.-J. Chen, and F.-C. Chien, "Dynamic particle tracking via temporal focusing multiphoton microscopy with astigmatism imaging," *Opt. Express* **22**, 27290–27299 (2014).
- ⁷¹L. Zhao, Y. Zhong, Y. Wei, N. Ortiz, F. Chen, and G. Wang, "Microscopic movement of slow-diffusing nanoparticles in cylindrical nanopores studied with three-dimensional tracking," *Anal. Chem.* **88**, 5122–5130 (2016).
- ⁷²Y. Ichikawa, K. Yamamoto, and M. Motosuke, "Three-dimensional flow velocity and wall shear stress distribution measurement on a micropillar-arrayed surface using astigmatism pty to understand the influence of microstructures on the flow field," *Microfluid. Nanofluid.* **22**, 73 (2018).
- ⁷³B. Huang, W. Wang, M. Bates, and X. Zhuang, "Three-dimensional super-resolution imaging by stochastic optical reconstruction microscopy," *Science* **319**, 810–813 (2008).
- ⁷⁴F. C. Zanacchi, Z. Lavagnino, M. P. Donnorso, A. Del Bue, L. Furia, M. Faretta, and A. Diaspro, "Live-cell 3d super-resolution imaging in thick biological samples," *Nat. Methods* **8**, 1047 (2011).
- ⁷⁵W. R. Legant, L. Shao, J. B. Grimm, T. A. Brown, D. E. Milkie, B. B. Avants, L. D. Lavis, and E. Betzig, "High-density three-dimensional localization microscopy across large volumes," *Nat. Methods* **13**, 359 (2016).
- ⁷⁶J. S. Biteen, E. D. Goley, L. Shapiro, and W. Moerner, "Three-dimensional super-resolution imaging of the midplane protein FtsZ in live caulobacter crescentus cells using astigmatism," *ChemPhysChem* **13**, 1007–1012 (2012).
- ⁷⁷H. P. Kao and A. S. Verkman, "Tracking of single fluorescent particles in three dimensions: Use of cylindrical optics to encode particle position," *Biophys. J.* **67**, 1291–1300 (1994).
- ⁷⁸S. R. P. Pavani, M. A. Thompson, J. S. Biteen, S. J. Lord, N. Liu, R. J. Twieg, R. Piestun, and W. E. Moerner, "Three-dimensional, single-molecule fluorescence imaging beyond the diffraction limit by using a double-helix point spread function," *Proc. Natl. Acad. Sci. U. S. A.* **106**, 2995–2999 (2009).
- ⁷⁹M. D. Lew, S. F. Lee, M. Badieirostami, and W. E. Moerner, "Corkscrew point spread function for far-field three-dimensional nanoscale localization of pointlike objects," *Opt. Lett.* **36**, 202–204 (2011).
- ⁸⁰A. Greengard, Y. Y. Schechner, and R. Piestun, "Depth from diffracted rotation," *Opt. Lett.* **31**, 181–183 (2006).
- ⁸¹S. R. P. Pavani and R. Piestun, "High-efficiency rotating point spread functions," *Opt. Express* **16**, 3484–3489 (2008).
- ⁸²G. Grover, S. Quirin, C. Fiedler, and R. Piestun, "Photon efficient double-helix PSF microscopy with application to 3d photo-activation localization imaging," *Biomed. Opt. Express* **2**, 3010–3020 (2011).
- ⁸³G. Grover, K. DeLuca, S. Quirin, J. DeLuca, and R. Piestun, "Super-resolution photon-efficient imaging by nanometric double-helix point spread function localization of emitters (spindle)," *Opt. Express* **20**, 26681–26695 (2012).
- ⁸⁴R. Berlich and S. Stallinga, "High-order-helix point spread functions for monocular three-dimensional imaging with superior aberration robustness," *Opt. Express* **26**, 4873–4891 (2018).
- ⁸⁵S. Jia, J. C. Vaughan, and X. Zhuang, "Isotropic three-dimensional super-resolution imaging with a self-bending point spread function," *Nat. Photonics* **8**, 302–306 (2014).
- ⁸⁶Y. Zhou, V. Zickus, P. Zammit, J. M. Taylor, and A. R. Harvey, "High-speed extended-volume blood flow measurement using pupil-engineered point-spread functions," *Biomed. Opt. Express* **9**, 6444–6454 (2018).
- ⁸⁷Y. Sun, J. D. McKenna, J. M. Murray, E. M. Ostap, and Y. E. Goldman, "Parallax: High accuracy three-dimensional single molecule tracking using split images," *Nano Lett.* **9**, 2676–2682 (2009).
- ⁸⁸J. Yajima, K. Mizutani, and T. Nishizaka, "A torque component present in mitotic kinesin Eg5 revealed by three-dimensional tracking," *Nat. Struct. Mol. Biol.* **15**, 1119–1121 (2008).
- ⁸⁹M. V. Berry and N. L. Balazs, "Nonspreading wave packets," *Am. J. Phys.* **47**, 264–267 (1979).
- ⁹⁰G. A. Siviloglou, J. Broky, A. Dogariu, and D. N. Christodoulides, "Observation of accelerating airy beams," *Phys. Rev. Lett.* **99**, 213901 (2007).
- ⁹¹Y. Shechtman, L. E. Weiss, A. S. Backer, S. J. Sahl, and W. E. Moerner, "Precise three-dimensional scan-free multiple-particle tracking over large axial ranges with tetrapod point spread functions," *Nano Lett.* **15**, 4194–4199 (2015).
- ⁹²Y. Shechtman, S. J. Sahl, A. S. Backer, and W. E. Moerner, "Optimal point spread function design for 3d imaging," *Phys. Rev. Lett.* **113**, 133902 (2014).
- ⁹³S. Quirin, S. R. P. Pavani, and R. Piestun, "Optimal 3d single-molecule localization for superresolution microscopy with aberrations and engineered point spread functions," *Proc. Natl. Acad. Sci. U. S. A.* **109**, 675–679 (2012).
- ⁹⁴A. V. Abraham, S. Ram, J. Chao, E. S. Ward, and R. J. Ober, "Quantitative study of single molecule location estimation techniques," *Opt. Express* **17**, 23352–23373 (2009).
- ⁹⁵G. Grover, S. R. P. Pavani, and R. Piestun, "Performance limits on three-dimensional particle localization in photon-limited microscopy," *Opt. Lett.* **35**, 3306–3308 (2010).
- ⁹⁶M. K. Cheezum, W. F. Walker, and W. H. Guilford, "Quantitative comparison of algorithms for tracking single fluorescent particles," *Biophys. J.* **81**, 2378–2388 (2001).
- ⁹⁷J. J. Moré, "The Levenberg-Marquardt algorithm: Implementation and theory," in *Numerical Analysis* (Springer, 1978), pp. 105–116.
- ⁹⁸F. Aguet, D. Van De Ville, and M. Unser, "A maximum-likelihood formalism for sub-resolution axial localization of fluorescent nanoparticles," *Opt. Express* **13**, 10503–10522 (2005).
- ⁹⁹M. Lindén, V. Čurić, E. Amselem, and J. Elf, "Pointwise error estimates in localization microscopy," *Nat. Commun.* **8**, 15115 (2017).
- ¹⁰⁰L. Gu, Y. Sheng, Y. Chen, H. Chang, Y. Zhang, P. Lv, W. Ji, and T. Xu, "High-density 3d single molecular analysis based on compressed sensing," *Biophys. J.* **106**, 2443–2449 (2014).
- ¹⁰¹S. J. Holden, S. Uphoff, and A. N. Kapanidis, "Daostorm: An algorithm for high-density super-resolution microscopy," *Nat. Methods* **8**, 279 (2011).
- ¹⁰²H. Babcock, Y. M. Sigal, and X. Zhuang, "A high-density 3d localization algorithm for stochastic optical reconstruction microscopy," *Opt. Nanosc.* **1**, 6 (2012).
- ¹⁰³E. A. Mukamel, H. Babcock, and X. Zhuang, "Statistical deconvolution for superresolution fluorescence microscopy," *Biophys. J.* **102**, 2391–2400 (2012).
- ¹⁰⁴Y. Wang, T. Quan, S. Zeng, and Z.-L. Huang, "Palmer: A method capable of parallel localization of multiple emitters for high-density localization microscopy," *Opt. Express* **20**, 16039–16049 (2012).
- ¹⁰⁵L. Zhu, W. Zhang, D. Elnatan, and B. Huang, "Faster storm using compressed sensing," *Nat. Methods* **9**, 721 (2012).
- ¹⁰⁶A. Barsic, G. Grover, and R. Piestun, "Three-dimensional super-resolution and localization of dense clusters of single molecules," *Sci. Rep.* **4**, 5388 (2014).
- ¹⁰⁷J. Huang, M. Sun, K. Gumpfer, Y. Chi, and J. Ma, "3d multifocus astigmatism and compressed sensing (3d macs) based superresolution reconstruction," *Biomed. Opt. Express* **6**, 902–917 (2015).
- ¹⁰⁸J. Huang, M. Sun, J. Ma, and Y. Chi, "Super-resolution image reconstruction for high-density three-dimensional single-molecule microscopy," *IEEE Trans. Comput. Imaging* **3**, 763–773 (2017).
- ¹⁰⁹M. P. Backlund, Y. Shechtman, and R. L. Walsworth, "Fundamental precision bounds for three-dimensional optical localization microscopy with Poisson statistics," *Phys. Rev. Lett.* **121**, 023904 (2018).
- ¹¹⁰M. Tsang, R. Nair, and X.-M. Lu, "Quantum theory of superresolution for two incoherent optical point sources," *Phys. Rev. X* **6**, 031033 (2016).